Effects of Horus Antenna Patterns on the Copolar Correlation of Weather Returns

Dušan Zrnić, *Life Fellow, IEEE*, David Schvartzman, *Senior Member, IEEE*, Robert D. Palmer, *Fellow, IEEE*, and Alexander V. Ryzhkov

***Abstract*— The effects of phased array antenna patterns on copolar correlation coefficient of polarimetric radar are analyzed. Analytic expressions are derived and used to quantify biases in the copolar correlation coefficient caused by mismatch of beam widths for horizontal and vertical polarizations. Misalignment in the beams' pointing direction is also considered. Measurements are made on an 8 × 8 panel of a polarimetric phased array radar (PPAR) under development by the Advanced Radar Research Center at the University of Oklahoma in collaboration with NOAA's National Severe Storms Laboratory. The all-digital radar is called Horus and some measurements on a partially populated antenna are presented.**

***Index Terms*— Phased array radar, polarimetric radar, all-digital radar, weather radar, antenna patterns.**

I. Introduction

PHASED Array Radar (PAR) may be a last step improvement in radar technology for observations of weather, both to serve scientific investigations and operational applications. It is considered for future weather radars because it can provide adaptive (i.e., where and when it matters) high-quality meteorological observations and thus advance understanding of atmospheric phenomena [1] and improve warnings and nowcasts. Upgrade of the National Network of weather surveillance radars (WSR-88D) to dual polarization caused a significant step increase in quality of quantitative precipitation estimation as well as capability to identify a wide variety of sources causing radar returns [2]. Therefore, dual-polarization capability has become a de facto requirement for modern weather radars including the PARs. Widely accepted polarization mode consists of transmission and reception of electromagnetic waves in both Horizontal (H) and Vertical (V) polarizations. In the Simultaneous Transmit Simultaneous Receive (STSR) mode, adopted by most operational and research weather radars, the H- and V-polarized waves are transmitted simultaneously thus creating an elliptically polarized wave. At the receiving antenna the returned waves are separated into channels for horizontal and vertical polarizations. Producing accurate polarimetric weather measurements with PARs in the STSR mode is challenging due to biases induced by the co- and cross-polar antenna patterns when the beam is pointed off the broadside [3] [4].

The magnitude of the correlation coefficient between the horizontally and vertically polarized returns, ρ_{hv} is a key parameter defining the quality of polarimetric radar measurements [2], [5]. The standard errors of the estimates of polarimetric variables are significantly reduced if ρ_{hv} of the weather signals exceeds 0.99 [2] – a basic requirement for polarimetric weather radars. Additionally, accurate measurements of ρ_{hv} are crucial for polarimetric detection of the melting layer and determination of its height [6] and for identification of the areas of hail and quantification of its size [7]. Therefore, the requirements for the ρ_{hv} measurements in the design of radars for weather observations are strict and important.

The S-Band mobile polarimetric all-digital Horus radar system was developed by the Advanced Radar Research Center (ARRC) at the University of Oklahoma (OU). Its purpose is to rapidly scan storm volumes while yielding high quality polarimetric observations. By design the Horus radar system is scalable and modular - thus suitable for initial deployments with a partially assembled antenna. The companion article describing the Horus system architecture is in this journal [8]. Considering that the polarimetric performance of a PAR is largely dictated by its far-field copolar and cross-polar radiation patterns, herein we analyze the patterns of one 8×8 element panel of the Horus antenna. Specifically, we investigate the impact of differences in the copolar H/V beams on the correlation coefficient (ρ_{hv}) estimates and evaluate these using measured patterns. An approximate analysis of the effect of the cross-polar patterns on ρ_{hv} is in [9]. Furthermore, we extrapolate the analysis to a full size (5×5 panels) Horus and a hypothetical 16×16 panel radar having a beamwidth of about 1^o as on the WSR-88Ds.

The analysis of the beam effects on ρ_{hv} assumes a *uniform distribution of scatterers* sizes in regions larger than the resolution volume (defined by the beam cross section and range depth of the sampling volume). Beams illuminating these scatterers cause quantifiable bias in ρ_{hv} useful for relative comparisons. This is unlike the effects on the returned

Manuscript received 20 January 2023; revised 5 May 2023; accepted 4 June 2023. Date of publication 7 June 2023; date of current version 15 August 2023. This work was supported in part by the National Oceanic and Atmospheric Administration (NOAA)/Office of Oceanic and Atmospheric Research through the NOAA–University of Oklahoma Cooperative Agreement under Grant NA16OAR4320115 and in part by the U.S. Department of Commerce. *(Corresponding author: Dušan Zrnić.)*

Dušan Zrnić is with the NOAA/OAR/National Severe Storms Laboratory, Advanced Radar Research Center, School of Meteorology and the School of Electrical and Computer Engineering, The University of Oklahoma Norman, OK 73072 USA (e-mail: Dusan.Zrnic@noaa.gov).

David Schvartzman and Robert D. Palmer are with the Advanced Radar Research Center and the School of Meteorology, The University of Oklahoma, Norman, OK 73072 USA.

Alexander V. Ryzhkov is with the Cooperative Institute for Severe and High-Impact Weather Research and Operations, Advanced Radar Research Center, The University of Oklahoma, Norman, OK 73072 USA, and also with the NOAA/OAR/National Severe Storms Laboratory, Norman, OK 73072 USA.

Digital Object Identifier 10.1109/TRS.2023.3283560

Fig. 1. The fully digital Horus mobile radar, with 25 antenna panels (8×8 dual-pol elements each). More details can be found in the Horus System article published in this journal [8].

powers (at H and V polarization), differential reflectivity or linear depolarization ratio. These, for example, are not biased by beams having equal cross section but different pointing direction. Bias by beams with different cross sections and corresponding gains can be accounted for through calibration and measurements (cross sections and gains). This is one reason we refrain from considering these biases here, the other is the concomitant increase in the article's length with trivial discourse. It is much harder to correct biases in polarimetric variables if the beam is pointed out of the array's cardinal planes [10].

II. The All-Digital Horus PAR

An all-digital phased array architecture is the most advanced and flexible PAR technology for enabling enhanced weather surveillance strategies envisioned to improve the temporal resolution and quality warnings on the basis of weather radar observations [9]. Important reasons (e.g., minimal attenuation, clear-air detectability) favor an S-band frequency (same as on WSR-88D). It can serve a wide community in atmospheric science if its antenna is large to form a sufficiently narrow beam. The growth of the wireless communications industry revolutionized electronic circuits enabling digitization (and control) at every element of an S-band array antenna [11]. NOAA is exploring digital radar technology [12] and had funded the ARRC to develop an all-digital PAR demonstrator [8].

The mobile Horus radar (Fig. 1) is a small S-band *engineering* demonstrator being built by ARRC. Significant aim of this project is to mitigate risks (i.e., maturity of the technology, maintainability, failure rates of components, quality of radar variables, feasibility/tradeoffs for rapid scans and adaptive scans) associated with all-digital phased array architectures and demonstrate its advanced capabilities. The radar has a 4.5° beamwidth suitable for showing functionality and overall scalability as well as limited atmospheric research about weather close to the radar. Element-level waveform and polarization flexibility, imaging, control/calibration methods, and power levels are compatible *by design* with a full-scale system for weather surveillance similar to the WSR-88D.

The all-digital array panel defined as an 8×8 mechanical and electrical subarray, is the primary building block. The panel's tube-based frame serves as mechanical support as well as conduit for liquid cooling. The "OctoBlades," eight per panel, house all electronics and slide into the panel frame to connect: a) the liquid cooling system, b) the backplane, and c) the antenna array itself through blind-mate connectors that pass-through cutouts in the backplane. The OctoBlades are the heart of the overall system implementation [13].

A centralized module on each panel is the SuperBlade, supporting the active electronic components. This module also serves the panel's analog backplane by distributing DC power, local oscillator signal, and a reference clock to each of the OctoBlades. The radar's wideband waveforms are switchable from dwell-to-dwell in the 2.7-3.1 GHz frequency band. The radiators are aperture-coupled, stacked-patch elements that provide high-quality polarimetric isolation (better than -45 dB cross-polarization suppression after calibration). By digitizing at the element level, we have shown that polarimetric calibration of the radar hardware can be robustly accomplished (see companion Horus article on calibration, [14]).

III. Effect of H/V Beam Mismatch on ρ_{hv}

Herein we present the effects of different beamwidth and pointing direction of the H and V beam on the copolar correlation coefficient (ρ_{hv}). We ignore contribution by sidelobes as well as by cross-polar patterns. To arrive at a solution, we make several assumptions and approximations (Appendix A) on the basis of which an objective comparison of effects is possible. Assumptions are: Uniformly distributed scatterers over a volume larger that the radar resolution volume V_6 [15] (see also the Appendix). Scatterers from V_6 contribute most to the returned signals. Range extent of V_6 is same for both polarizations. This is expected from matched H and V channels. We consider patterns with elliptical cross sections that may differ in widths and pointing directions. Therefore, we have defined the widths as follows (Appendix). The two-way width of the pattern for horizontal polarization along the arc (angle) χ is $\sigma_{h\chi}$; $\sigma_{h\gamma}$, is the width along the vertical arc (angle) γ; for vertical polarization the corresponding widths are $\sigma_{v\chi}$ and $\sigma_{v\gamma}$. The two-way width (σ_θ) of a Gaussian pattern is related to the one-way 3 dB beamwidth θ_1 via $\theta_1 = 4\sqrt{\ln(2)}\sigma_\theta$ [15]. Identical relation holds for the vertical (meridional) width and horizontal (lateral) width. Because the beams are extremely narrow, the overlapping and significant parts of the beam cross section can be assumed to be almost flat and parallel to the polarization plane (Appendix). In this coordinate system we denote with χ and γ the perpendicular angles in the beam cross section plane (Appendix Fig. 12) and integrate the relevant patterns to compute the decorrelation by the beam effects.

The angular (solid angle) cross sections of two overlapping beams with different widths and pointing directions are in Fig. 2.

For Gaussian patterns f_h^2 and f_v^2, the expression for the correlation coefficient (Appendix) is

$$\rho_{hv} = \frac{\langle s_{hh} s_{vv} \rangle}{\left\langle |s_{hh}|^2 \right\rangle^{1/2} \left\langle |s_{vv}|^2 \right\rangle^{1/2}} \frac{\int f_h^2 f_v^2}{\left(\int f_h^4 \right)^{1/2} \left(\int f_v^4 \right)^{1/2}}, \qquad (1)$$

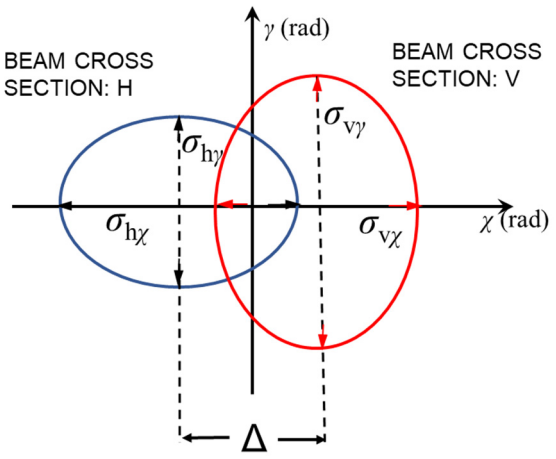

Fig. 2. Angular cross section of two overlapping elliptical beams whose centers are offset by Δ.

where the scattering coefficients at H and V polarizations are s_{hh}, s_{vv}, and $\langle\rangle$ denotes ensemble average. In (1) the intrinsic correlation coefficient, ρ_{hvi} is the first term, that is

$$\rho_{hvi} = \frac{\langle s_{hh} s_{vv}\rangle}{\langle|s_{hh}|^2\rangle^{1/2}\langle|s_{vv}|^2\rangle^{1/2}} \tag{2}$$

and the second term is the patterns' induced bias. The ratio of the biased ρ_{hv} (left side of (1)) to the intrinsic correlation coefficient (2) defines the fractional bias ξ caused by antenna pattern mismatch

$$\xi = \frac{\rho_{hv}}{\rho_{hvi}} \tag{3}$$

or

$$\xi = \frac{\int f_h^2 f_v^2}{\left(\int f_h^4\right)^{1/2}\left(\int f_v^4\right)^{1/2}}. \tag{4}$$

In this definition $\xi = 1$ signifies unbiased estimate.

Let the offset of H polarization pattern from zero along the χ angle be - Δ /2 and that of V polarization pattern be Δ/2 (Fig. 2). Then the equations for one-way patterns are

$$f_h^2(\chi,\gamma) = \frac{1}{4\pi\sigma_{h\chi}\sigma_{h\gamma}}\exp\left[-\frac{(\chi+\Delta/2)^2}{4\sigma_{h\chi}^2}\right]\exp\left[-\frac{\gamma^2}{4\sigma_{h\gamma}^2}\right] \tag{5a}$$

and

$$f_v^2(\chi,\gamma) = \frac{1}{4\pi\sigma_{v\chi}\sigma_{v\gamma}}\exp\left[-\frac{(\chi-\Delta/2)^2}{4\sigma_{v\chi}^2}\right]\exp\left[-\frac{\gamma^2}{4\sigma_{v\gamma}^2}\right]. \tag{5b}$$

The integrals of (A5) as stipulated in (A4) are over χ and γ and for the case of interest (narrow beams) can be extended from -∞ to +∞ in both dimensions (Appendix). Take circular cross sections of different size for the H/V polarizations so $\sigma_{h\chi} = \sigma_{h\gamma} = \sigma_h$ and $\sigma_{v\chi} = \sigma_{v\gamma} = \sigma_v$, then integrate (A4) to obtain the closed form solution for ξ

$$\xi = \frac{2\sigma_h\sigma_v}{\sigma_h^2+\sigma_v^2}\exp\left(-\frac{\Delta^2}{4(\sigma_h^2+\sigma_v^2)}\right). \tag{6}$$

By inspection we see that with zero offset and same beam widths $\xi = 1$. Hence there is no bias and the lobes are perfectly matched.

For elliptical beams the f_h^2 and f_v^2 are

$$f_h^2(\chi,\gamma) = \exp\left[-\frac{(\chi+\Delta_1/2)^2}{4\sigma_{h\chi}^2} - \frac{(\gamma+\Delta_2/2)^2}{4\sigma_{h\gamma}^2}\right], \tag{7}$$

and

$$f_v^2(\chi,\gamma) = \exp\left[-\frac{(\chi-\Delta_1/2)^2}{4\sigma_{v\chi}^2} - \frac{(\gamma-\Delta_2/2)^2}{4\sigma_{v\gamma}^2}\right], \tag{8}$$

where Δ_1, Δ_2 are the offsets in the χ and γ directions. Use of (7) and (A8) in (1) yields the bias

$$\xi = 2\sqrt{\frac{\sigma_{h\chi}\sigma_{v\chi}}{\sigma_{h\chi}^2+\sigma_{v\chi}^2}}\exp\left(-\frac{\Delta_1^2}{4(\sigma_{h\chi}^2+\sigma_{v\chi}^2)}\right)\cdot \sqrt{\frac{\sigma_{h\gamma}\sigma_{v\gamma}}{\sigma_{h\gamma}^2+\sigma_{v\gamma}^2}}\exp\left(-\frac{\Delta_2^2}{4(\sigma_{h\gamma}^2+\sigma_{v\gamma}^2)}\right). \tag{9}$$

For the WSR-88D the ρ_{hv} bias is specified at less than 0.006. Because this bias contains the effects of the whole system, we choose one half (0.003) to illustrate what a desirable value for a PAR antenna should be. Consider circular beam cross sections and geometry as in Fig. 2. Then the fractional bias should satisfy $0.997 < \xi < 1.003$. By including this inequality in (6) we can determine the conditions it imposes on the multiplying and exponential terms. Note that the multiplying term has a maximum of 1 if $\sigma_h = \sigma_v$. Further, the strictest condition on the fractional bias is if it is closest to 1 (where 1 means no bias). This and because the exponential term is 1 if $\Delta = 0$ means the worst (most demanding) condition for the multiplying term is

$$0.997 < \frac{2\sigma_h\sigma_v}{\sigma_h^2+\sigma_v^2} \le 1. \tag{10}$$

Clearly the upper condition for the exponential term is also 1 as it cannot be any larger. Therefore, the worst (most demanding) lower limit for this term is

$$0.997 < \exp\left(-\frac{\Delta^2}{4(\sigma_h^2+\sigma_v^2)}\right). \tag{11}$$

One can see that in this case the condition (10) depends on σ_h/σ_v and (11) depends on one more parameter, Δ/σ_v. For elliptic beams the following four parameters $\sigma_{h\chi}/\sigma_{v\chi}$, $\Delta_1/\sigma_{v\chi}$, $\sigma_{h\gamma}/\sigma_{v\gamma}$, and $\Delta_2/\sigma_{h\gamma}$ determine the bias in ρ_{hv}.

Next for simplicity and illustration assume matched pointing directions so that $\Delta = 0$ in (6) and the mismatch in beam widths is

$$\sigma_v = (1\pm\varepsilon)\sigma_h, \tag{12}$$

where ε is a number much smaller than 1. Inserting (12) into (6) one obtains the following relation,

$$\frac{2(1\pm\varepsilon)\sigma_h^2}{\sigma_h^2+(1\pm\varepsilon)^2\sigma_h^2} = \frac{2(1\pm\varepsilon)}{1+(1\pm\varepsilon)^2} \ge \xi. \tag{13}$$

Assuming beam mismatch is the only cause of ρ_{hv} bias we need to find the largest ε for which the inequality (13) holds. The solution for $(1\pm\varepsilon)$ is

$$(1 \pm \varepsilon) = \frac{1 \pm \sqrt{1-\xi^2}}{\xi}, \tag{14}$$

consequently

$$\pm\varepsilon = \frac{1 \pm \sqrt{1-\xi^2}}{\xi} - 1. \tag{15}$$

As example assume a drop in correlation from 1 to 0.997, hence $\xi = 0.997$ and (rounded) $\varepsilon_{1,2} = \pm 0.08$. Then if the 3 dB beamwidth (H polarization) $\theta_{1h} = 1°$, the θ_{1v} would be constrained to between 0.92 and 1.08°. This can be also cast as difference at an L (dB) level below the peak of the pattern as follows. Note that the angle with respect to beam center at L (dB) below the peak is

$$\theta_L = \frac{\theta_1\sqrt{2L}}{4\sqrt{\ln 2[10\log(e)]}} = \frac{\sigma_h\sqrt{2L}}{\sqrt{10\log(e)}}. \tag{16}$$

At mismatched beams (10) holds and we can compute the difference δ_{20} (dB) between matched ($\varepsilon = 0$) and not matched ($\varepsilon \neq 0$) patterns at the L level as

$$\delta_{20} = L\left[1 - \frac{1}{(1+\varepsilon)^2}\right] \text{or} L\left[\frac{1}{(1-\varepsilon)^2} - 1\right]. \tag{17}$$

Thus if $1+\varepsilon = 1.08$ and $L = 20$ dB, the $\delta_{20} = 2.85$ dB. If $\rho_{hv} = 0.999$, $\delta_{20} = 1.7$ dB so it is fair to state that at the 20 dB level the difference in the patterns should be less than 2 dB, provided that at the peak the gains have been matched.

In a practical array it may not be possible to have a perfectly circular beam cross section but an approximately elliptic one, especially in the case of a phased array radar pointing off broadside. Let us look at elliptic Gaussian patterns with widths $\sigma_{h\chi}$, $\sigma_{h\gamma}$ and $\sigma_{v\chi}$ and $\sigma_{v\gamma}$ as explained earlier and depicted in (Fig.2), but with both H and V lobes centered at the origin. Then the fractional bias ξ becomes (Appendix)

$$\xi = \frac{2\left(\sigma_{h\chi}\sigma_{v\chi}\sigma_{h\gamma}\sigma_{v\gamma}\right)^{1/2}}{(\sigma_{h\chi}^2 + \sigma_{h\gamma}^2)^{1/2}(\sigma_{v\chi}^2 + \sigma_{v\gamma}^2)^{1/2}}. \tag{18}$$

Next consider a special case where the lengths of the longer axis are equal and also the lengths of the shorter axis are equal. That is $\sigma_{hx} = \sigma_{vy}$ and $\sigma_{vx} = \sigma_{hy}$. These are implied by the symmetry of the patch's shape. Moreover, if centers of the two cross sections coincide then rotation by 90° of one of these would produces the other one and (18) reduces to

$$\xi = \frac{2\sigma_{h\chi}\sigma_{v\chi}}{\left(\sigma_{h\chi}^2 + \sigma_{v\chi}^2\right)}. \tag{19}$$

This equation represents the estimated bias by antenna patterns with elliptical beam cross-sections. By setting $\Delta = 0$ in (6) we see that (19) is same as bias by circular beams with different widths. The reason that the two geometries yield the same result is in the underlying assumptions about the scatterers. These are uniformly distributed over a volume much larger than the radar resolution volume.

In the next section, we use measured patterns of an 8×8 active Horus antenna panel to estimate their influence on ρ_{hv} estimates.

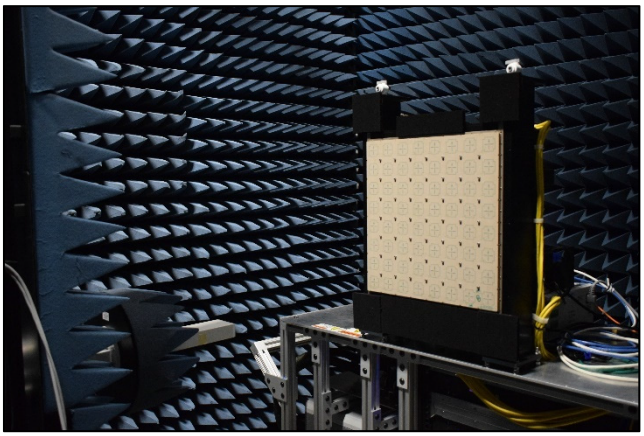

Fig. 3. Near-field scanner setup to fully characterize the H and V antenna patterns of the Horus panel.

IV. Evaluation of Horus Antenna Panel Patterns

One antenna panel of the scalable Horus array was fully populated with electronics that make up the transmit and receive signal paths and was assembled in a near-field chamber for testing (Fig. 3). This setup enables the panel to operate as a radar (albeit with a small aperture) so that we can test its performance in the STSR mode for dual-polarization measurements. The near-field scanner is comprised of two motorized Velmex BiSlide assemblies, one Velmex VXM Stepper Motor Controller, an S-band open-ended rectangular waveguide probe (OEWP), a Newport "optical breadboard" base, and RF absorber. These features allow measurement of antenna patterns in the H and V polarizations. Two-axis motion is achieved by controlling one stepper motor per axis. The motor controller takes in formatted commands and drives the stepper motors to achieve the desired movements. The S-band OEWP is mounted to the near-field scanner. The probe is covered with a collar of RF absorber. The near-field scanner is designed so that the system's (0,0) position is in the exact geometric center of the array face.

Near-field calibration is accomplished using the so-called park-and-probe technique to measure amplitude and phase of fields radiated by each antenna element, generate and apply alignment weights, and then verify the resulting alignment. A full set of transmit patterns requires four separate data collections, one for each combination of array polarization and OEWP orientation (0° or 90°). Although the panel hardware is capable of dual-polarized transmit operation, the OEWP is linearly polarized. Therefore, it is impossible to separate the H- from the V transmit response if transmitting both polarizations. Receive patterns can be collected with only two data sets. The panel hardware can receive both polarizations simultaneously and feedback the data separately. Multiple beam angles can be collected simultaneously in the receiver. Considering that a thorough alignment procedure was conducted and resulting H/V beam alignment was verified, hereafter, we neglect misalignment and consider only the beam shape mismatch. Beam shapes are determined by the design of the microstrip patches exciting each polarization and are more challenging to correct after the array is designed and

TABLE I
MEASURED PATTERN WIDTHS (BORESIGHT)

Pol. \ Level	-3 dB	-10 dB	-20 dB
H (χ)	12.574°	20.964°	25.662°
H (γ)	12.558°	20.802°	25.42°
V (χ)	12.556°	21.052°	25.716°
V (γ)	12.581°	21.112°	25.928°
Bias ξ	1.0	0.99998	0.99996

manufactured (in contrast to alignment). A deeper investigation on the impact of H/V beam misalignment on polarimetric PAR measurements is in [16].

Determining the far-field pattern of an antenna from near-field measurements requires a mathematical transformation and correction for the characteristics of the measuring antenna (i.e., the probe). We apply the near-field to far-field transformation via mathematical expressions derived by [17] to estimate the antenna far fields, similar to the procedure in [14].

Field transformations expressions are applied to the Horus near-field measurements to predict the far-field antenna patterns of this 8×8 array (i.e., one Horus panel), as in [18]. Normalized co-polar H and V far-field patterns are presented in Fig.4. Dotted contours on the copolar H and V patterns indicate the half-power beamwidth (-3 dB).

A comparison of these patterns indicates excellent mainlobe agreement between the H and V polarizations up to about -20 dB. The sidelobe structure for each polarization appears to be symmetric about the mainlobe for the horizontal and vertical cuts. A small difference ($\leq$0.7 dB) is observed between peak sidelobe levels in the H and V patterns. This may be caused by finite array effects such as diffraction and mutual coupling [19]. Similarly, the diagonal plane cuts show well matched H and V mainlobes (up to about -20 dB), although sidelobe levels are lower (as expected) due to the rectangular antenna geometry.

To evaluate the impact of these far-field patterns on ρ_{hv} (eqs.12 to 17), the beamwidths from cross sections at -3, -10, and -20 dB levels are extracted from the measurements and presented in Fig. 5. The widths measured in χ and γ at the -3, -10, and -20-dB levels are summarized in Table I.

Next, we compute the fractional bias ξ that the panel's mainlobe would inflict to the ρ_{hv} estimates. We can use (18) for that purpose by substituting the values from Table I because the Gaussian model allows use of widths from an arbitrary level below the mainlobe peak. Our results from the three levels (Table I, last row) for all practical purposes validate this assumption. The slight difference between ξ computed from the width at the – 3dB level and the widths at the -10 dB or -20 dB level are negligible. Moreover, the difference ξ(-3) - ξ(-L) increases with the increase in the level's magnitude L. This is likely due to the increase in deviation of the mainlobes shapes from the Gaussian at larger levels below the peak. Therefore, it is appropriate to take the widths at the -20 dB level as these impose more stringent requirement. This also follows from the fact that statistical errors in ρ_{hv} are not affected if SNR is larger than 20 dB [2].

Now we estimate the ρ_{hv} bias a PAR may cause if it has a 1° beamwidth as on the WSR-88D [15]. For that we take the widths at the -20 dB level and assume that the same absolute deviation from the mean width as in the one panel case would occur. The mean for the panel from table I forth column is 25.681° and the mean width for the 1° beam width antenna at the -20 dB level from (16) is 1.825°. Then the ξ(-20) of the 1° antenna from (18) is 0.9874 corresponding to a bias of 0.0126. For this (out of specification) value to occur all panels on the antenna would have to cause identical bias that adds "coherently". It is more likely that the panels would differ and the deviation of the widths from the mean would be random. Let us consider that case and assume the antenna consists of 16×16 panels. Then the variations of the widths would be approximately 4 times smaller than the deviations corresponding to the widths at the -20 dB level in Table I. The resulting $\xi = 0.9993$ and the corresponding bias of 0.0007 is negligible. We do not know if coherent or random addition of widths fluctuations will apply to the fully populated Horus antenna. Nonetheless, we plan to determine the bias Horus mainlobes impose once the antenna is assembled and pattern measurements are made in the ARRC's recently installed near-field scanner [14]. It may be possible to extrapolate these measurements to ones expected on a 1° beamwidth Horus type antenna.

The results derived here are obtained using a single Horus panel. From the expressions derived in the previous section and the measured widths, we estimate that the antenna will introduce at least an order of magnitude lower bias in ρ_{hv} than the requirement for polarimetric observations. Although a larger aperture would result in a narrower beam, it is expected that the H/V beam shapes will be preserved providing that accurate alignment calibration is performed.

V. PATTERN PERFORMANCE OFF BORESIGHT

It is known that co- and cross-polar antenna patterns of polarimetric PAR induce biases in the polarimetric variables, which increase as the beam is steered away from the broadside [20], [21]. Here in subsection *A* we present panel patterns off broadside and associated bias in ρ_{hv}. In *B* we consider a full-size Horus antenna and the bias it induces in ρ_{hv} as function of the pointing direction, and in *C* we present data obtained with an 1×5 panels Horus antenna.

A. Panel Patterns off Broadside

We consider Horus panel patterns electronically steered along the vertical principal plane. Specifically, a set of 15 independent measurements were taken per polarization as the beam is steered from -42° to 42° at 6° steps in elevation. In these measurements, the S-band probe transmits, and the Horus array receives. First, the probe was aligned to transmit horizontal polarization, then, to transmit vertical polarization. Co- and cross-polar antenna patterns were collected for each polarization and steering angle.

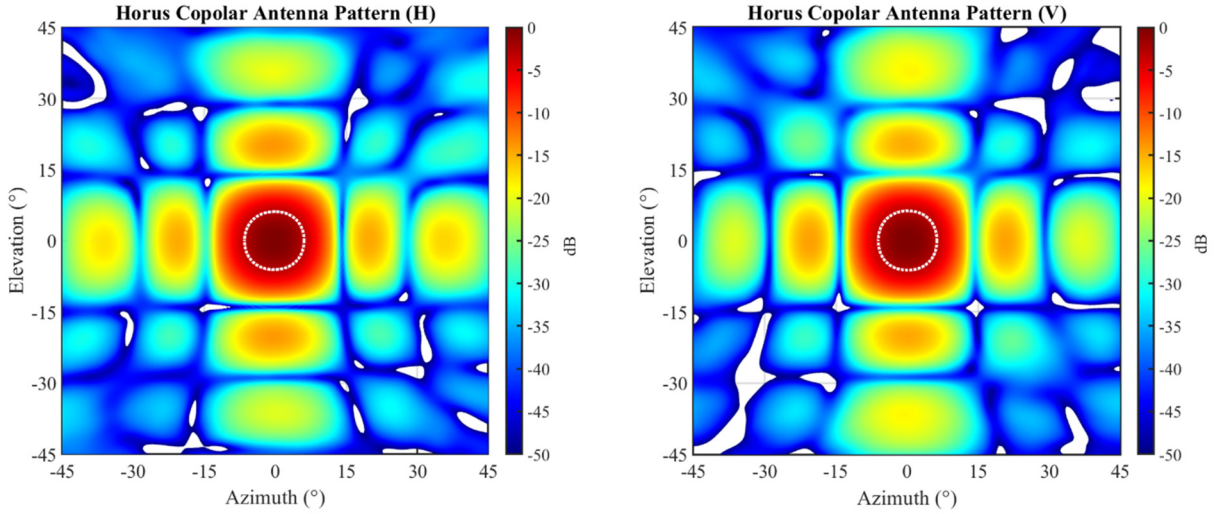

Fig. 4. Normalized (left) H and (right) V far-field Horus panel patterns derived using the near-field to far-field transformation.

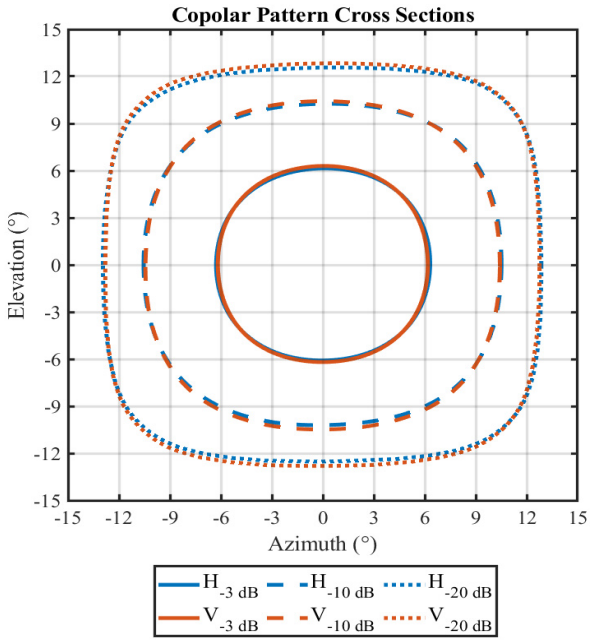

Fig. 5. Beam cross-sections at the -20, -10, and -3-dB level below the peak.

For each measurement, the beam cross-section at the half-power beamwidth is extracted and the pattern widths in χ and γ are measured. Measured beam cross-sections are shown in Fig. 6. The H and V cross-sections are represented with dashed and dotted lines. As expected, when the beam is steered away from the broadside, the pattern width increases approximately as $1/\cos(\theta)$, were θ is the steering angle. At broadside, the widths are $\sim$12.6°, and at the elevation steering angles of $\pm$42°, widths are $\sim$16°.

Qualitative comparison of the H and V cross-sections indicates that widths are well matched up to about $\pm$30°. Beyond these steering angles there seems to be a small pointing offset between H and V, the worst one being $< 0.1°$. Nevertheless, beam shapes appear to change similarly in general, which means that biases induced by the copolar patterns in ρ_{hv} are small. Beam widths measured at the -3 dB level are shown in Fig. 7.

It is apparent that the V pattern beamwidth increases more than the other pattern's beamwidths along γ, by about 1° at the $\pm$42° steering angles (Figs. 6 and 7). We hypothesize the reason is that the V patterns are aligned with the steering plane (vertical), which in a small array (8×8) may cause larger differences in the pattern shapes due to diffraction effects [22]. These measured beamwidths are used in (18) to estimate copolar antenna biases introduced by the Horus antenna in ρ_{hv}, shown in Fig. 8. Results indicate that biases are smaller than 0.0005) within the elevation (θ) span of $\pm$ 20°. They increase slightly as the beam is steered to $\pm$42° where the maximum of $\sim$0.0015 occurs. This is about half of the desired ρ_{hv} bias stated earlier (0.003). Measurements in the azimuth plane yielded very similar results hence are not presented.

B. Horus Antenna Patterns off Broadside

Although panel patterns were only measured in the elevation plane, the intent is to evaluate the performance of Horus PAR in a larger scan sector, steering the beam in two dimensions. Further, it is of interest to evaluate the performance of the full Horus array (4×4 active panels, 32×32 elements). Herein, we use element pattern measurements obtained in the ARRC's precision anechoic chamber and in the spherical far-field scan mode. From these we quantify biases of the full Horus array as the beam is steered in azimuth $\pm$45° and in elevation from 0° to 20°. A simulation following the approach proposed by [10] and [16] is used. It combines the effects of measured radiation patterns with simulated time-series signals, applying the well-established backscattering matrix model [23]. The model includes bulk statistical properties of scatterers within a resolution volume coupled with electromagnetic wave propagation and radar system effects. Effects from both the copolar and cross-polar antenna radiation patterns are considered. Simulation results are shown in Fig. 9.

It can be seen that biases induced by the Horus antenna in ρ_{hv} agree with those in Fig. 8 (along the vertical principal

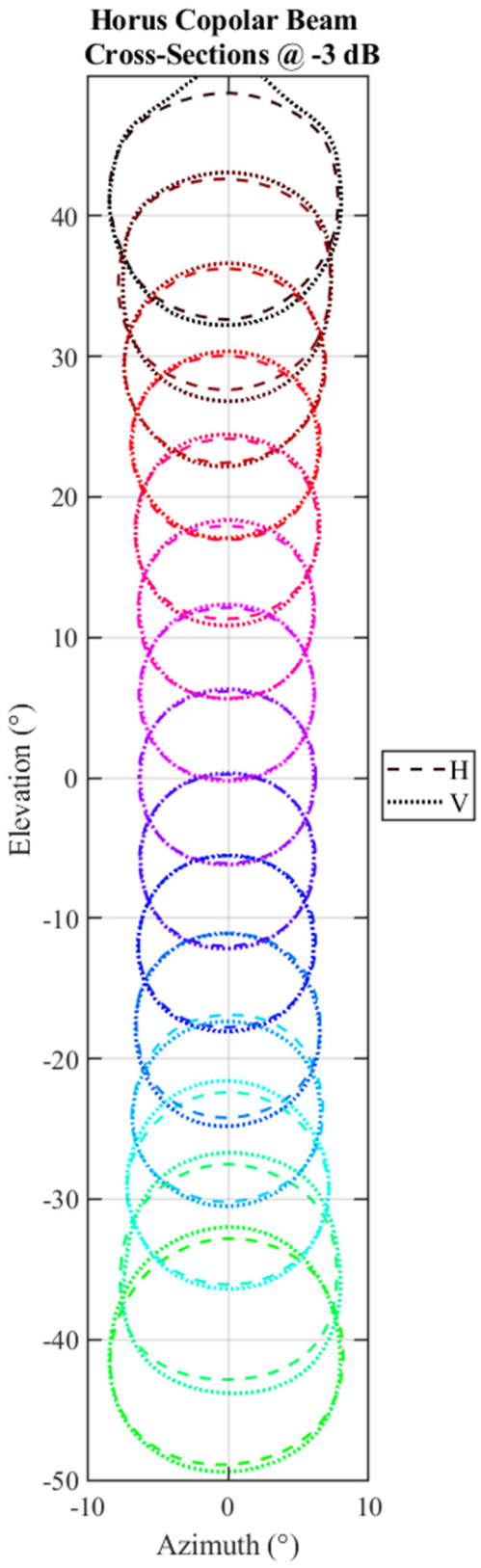

Fig. 6. Beam cross-sections at -3 dB as a function of steering angle, derived from NF measurements obtained using the setup presented in Fig. 3. The beams are steered in elevation, going from -42° to +42°. Dashed lines correspond to H and dotted lines to V.

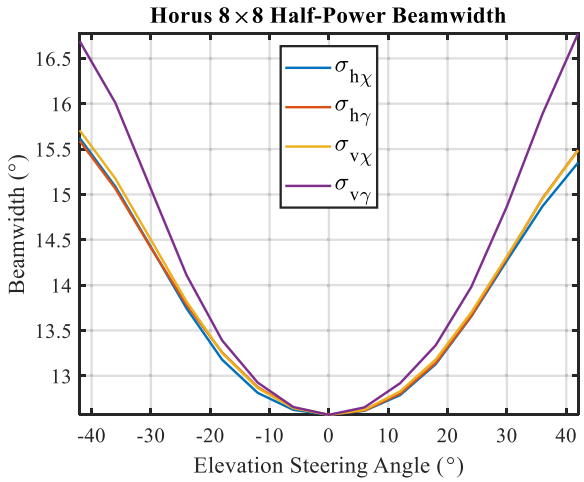

Fig. 7. Beamwidths measured from the cross-sections in Fig. 6. Note that the curves for $\sigma_{h\gamma}$ and $\sigma_{v\chi}$ are partially overlapping.

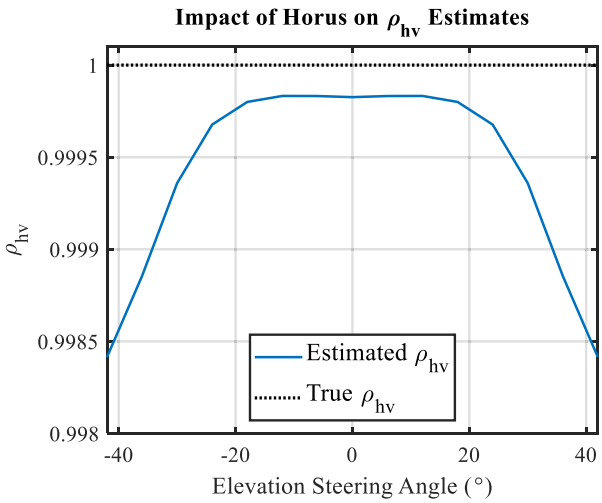

Fig. 8. Impact of copolar Horus panel antenna patterns on ρ_{hv} derived using (18) and the measured widths shown in Fig. 7.

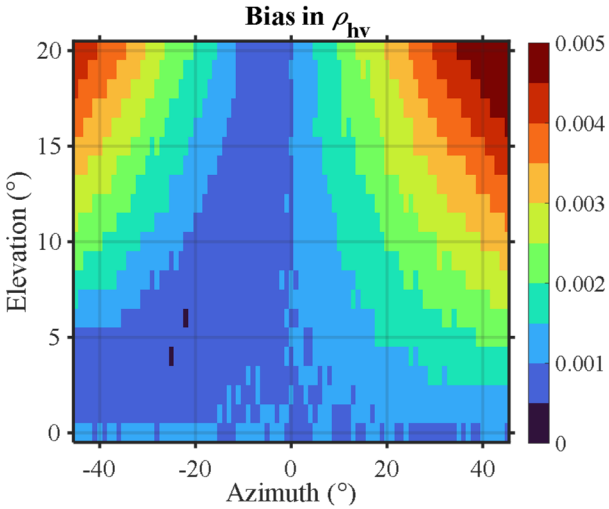

Fig. 9. Antenna-induced biases in ρ_{hv} as a function of steering angle, derived from measured element patterns for the active part of the full Horus array (4×4 panels). Note that biases induced are below the requirement (i.e., bias in $\rho_{hv} \leq 0.006$) through the scan sector of interest.

plane, where cross-polar patterns are < -50 dB), and are below the requirement [24] (i.e., bias in $\rho_{hv} \leq 0.006$) through the entire scan sector. This is due to the well-matched copolar beam patterns and the ultra-low cross-polarization levels of the Horus antenna [25] ($\leq$ -50 dB in the principal planes of both the full antenna and the panel). The integrated main lobe

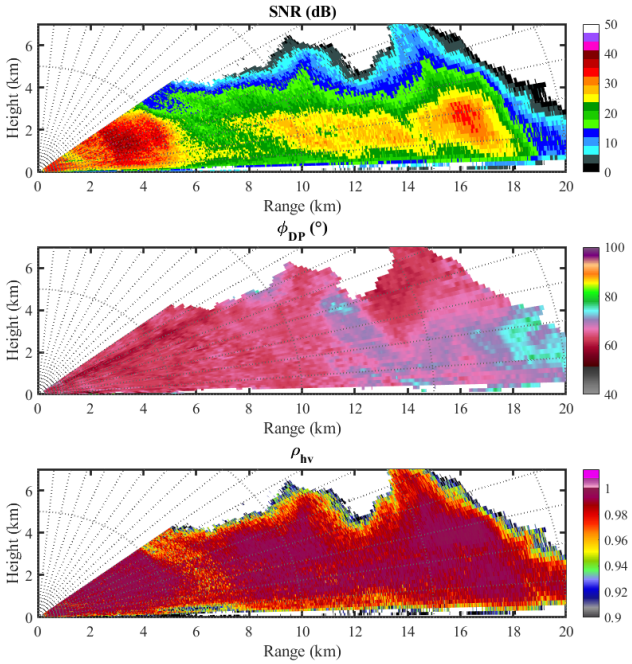

Fig. 10. Polarimetric weather measurements from a 5×1 panel Horus array (40×8 elements). Data were collected on 16 February 2023 at approximately 1:14:22 Z pointing at 190° azimuth. Panels are (top) SNR, (middle) Φ_{DP}, and (bottom) ρ_{hv}.

power to cross polar pattern power measured on the panel is 47.9 dB.

In summary, our quantitative analysis based on measured antenna patterns suggests that any adverse impact of the Horus antenna on ρ_{hv} estimates will be negligible. We expect that the shapes of H and V beams are preserved for the full Horus array to produce high-quality polarimetric weather measurements.

C. Evaluation of Horus ρ_{hv} Estimates

On the evening of 16 February 2023, the Horus radar was deployed near the Radar Innovations Laboratory in Norman, OK. Soon after, at approximately 1:14:22 Z, a quasi-linear convective system of storms was moving South-West to North-East passing south of Norman. Severe thunderstorm, flash flood, and tornado warnings were issued by National Weather Service (NWS) forecasters throughout the event[1],[2]. We collected polarimetric data from this event with the Horus radar for approximately 30 minutes.

Five Horus antenna panels (5×1) with corresponding electronic components (i.e., transmit/receive chains) were assembled into a vertical column of the Horus array structure at that time. We performed polarimetric calibration using the mutual coupling technique [26] and collected meteorological data for engineering evaluation. We scanned the beam in the vertical principal plane through a convective storm cell, going from 0° to 30° in 0.5° increments and obtained fields of the radar variables. A pulse-repetition time (PRT) of 1 ms with 128 samples per dwell was used, resulting in a scan time of ~8 s. Pulse compression waveforms with non-linear frequency

[1]See: https://www.spc.noaa.gov/exper/archive/event.php?date=20230215

[2]https://nwschat.weather.gov/lsr/#/202302152220/202302160831/0100

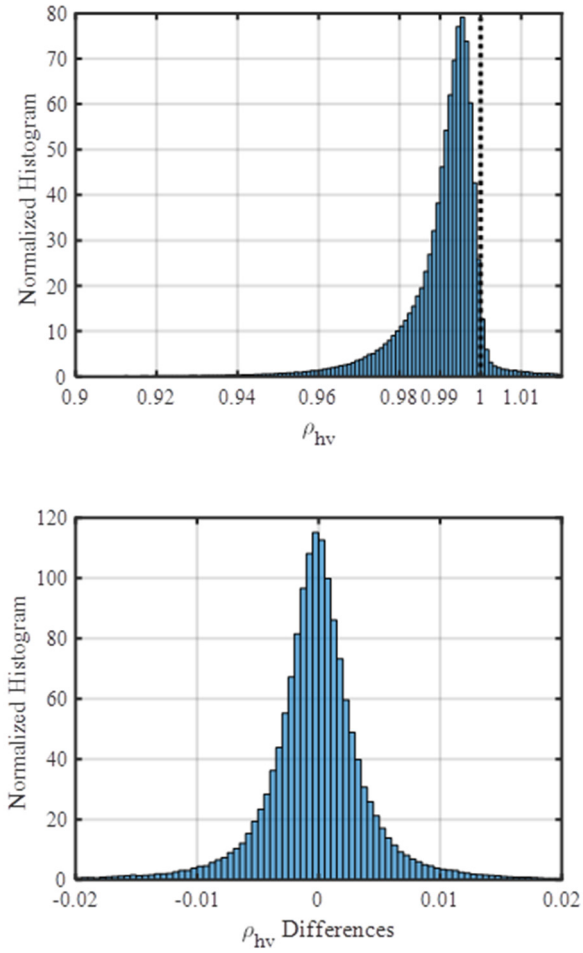

Fig. 11. Histogram of (top) ρ_{hv} values, and (bottom) differences between two consecutive fields of ρ_{hv}. Note that an SNR treshold of 20 dB is used to select data used in these histograms.

modulation were used, with a pulse width of 80 μs and a bandwidth of 5 MHz. Note that the progressive pulse compression technique was implemented to mitigate the pulse-compression blind range [27], [28]. Range-time samples were produced at a rate of 15.625 MSPS, resulting in a range sampling interval of approximately 10 m.

Pertinent to this paper are the signal-to-noise ratio (SNR), the correlation coefficient and the differential phase (Φ_{DP}) because it is the argument of the correlation coefficient; these are shown in Fig. 10. A qualitative analysis of the fields shows SNR values going up to approximately 40 dB at close range. Generally smooth fields of estimates were produced, as expected from volumetric scatterers encountered in precipitation systems that generally exhibit spatial continuity. Changes in Φ_{DP} are consistent with those from dish-based weather radars, whereby larger increases are observed in regions with high reflectivity (i.e., proportional to SNR at constant ranges). This is caused by the change in phase encountered by H and V waves as they traverse a precipitation core, where raindrops tend to be larger in the horizontal dimension (due to gravity and drag force), and therefore the H wave propagates slower than V (i.e., larger phase change) producing Φ_{DP} increases along range. The field of ρ_{hv} appears to have most values close to 1, indicating most

scatterers are of the same type (i.e., liquid raindrops or frozen hydrometeors). Regions with lower ρ_{hv} values may indicate mixed precipitation (e.g., water and ice), or a more general mixture of particles (e.g., debris).

To quantify polarimetric Horus performance, we present histograms of ρ_{hv} and of differences between fields of ρ_{hv} derived from consecutive scans, in Fig. 11. To mitigate estimation biases, only data with SNR $\geq$ 20 dB are selected. Histograms are normalized to approximate a probability density function. The height of each bar represents the ratio of the number of observations in bin divided by the product of the total number of observations and the width of a bin (in this case 0.0005). The area of each bar is the relative number of observations, and the sum of the bar areas is less than or equal to 1. The top histogram shows that most ρ_{hv} vales are concentrated between 0.99 and 1. This indicates H and V beams are well matched in shape, therefore antenna-induced biases are negligible. This is consistent with our analysis presented in Section IV. Furthermore, a zero-mean histogram is produced using differences between fields of ρ_{hv} from consecutive scans. The distribution appears to be a bilateral exponential or (Laplace distribution), with a standard deviation of 0.0085. This indicates stability on the system. Although standard errors in ρ_{hv} are mostly dependent of SNR, dwell time, and spectrum width, these histograms show that the Horus radar can produce polarimetric estimates of high quality.

VI. Conclusion

This article presents progress towards evaluating the performance of the Horus radar for polarimetric weather observations. Horus is a digital, polarimetric, S-band phased array radar being developed at the ARRC with support from NOAA. The Horus antenna aperture consists of a 5×5 arrangement of panels (of which not all are active), each with 8×8 antenna elements. With approximately 1024 active elements in total (4×4 panels), this proof-of-concept all digital system will have a 3-dB beamwidth of 4.5°. The Horus radar system has been integrated and initial deployments for polarimetric weather measurements are ongoing.

A theoretical evaluation of the mismatch between H and V beams was presented, with a focus on its impact on the copolar correlation coefficient (ρ_{hv}). Two mismatch parameters were considered: a pointing offset between beams and the ratio between the 3-dB widths in x and y (for H and V). Assuming magnitude and phase alignment is performed, and relatively narrowband waveforms are used (i.e., no beam squinting), the pointing offset would be mitigated. However, the widths of the H and V beams are determined by the element patterns and may be more challenging to adjust. Therefore, we derived theoretical expressions assuming no pointing offset but potentially different H/V beam widths.

In our measurements deviations between the widths at -20 dB below the peak are larger than at higher levels and are easier to estimate than deviations at the – 3dB level. Therefore, and because ρ_{hv} is not affected at SNRs larger than 20 dB, the widths at -20 dB from the mainlobe peak approximate better the effects on bias. Using these widths, we estimate that a complete Horus antenna would cause insignificant bias. We extrapolated the results to a Horus type PAR with a beamwidth of 1° like on the WSR-88D. The result indicates that if the deviations of single panel pattern widths sum coherently the bias would be unacceptable. Nevertheless, if these biases are incoherent then the resulting bias by the 1° antenna would satisfy the requirements. Incoherent bias means that the variations of the widths from panel to panel are independent which is more likely. Otherwise, all panels would have identical "flaws" and alignment error of panels on the antenna structure would be same.

Using near-field measurements from a fully populated active Horus antenna panel, we derived cuts of the antenna patterns in the x and y directions and for both H and V polarizations. A qualitative comparison of the H and V patterns indicates there is a high level of similarity. Moreover, the measure integrated copolar power of the panel to the cross polar power at broadside and within the main lobe is 47.9 dB. This and our quantitative analysis of the two (H, V) main lobe patterns, based on their measured widths, suggests that the impact of the Horus antenna on ρ_{hv} estimates will be negligible. We expect that the shapes of H and V beams are preserved for the full Horus array and thus will enable high-quality polarimetric weather measurements.

We collected polarimetric weather data with the 5×1-panel Horus array and evaluated its performance on the estimation of ρ_{hv}. Relatively smooth fields of polarimetric weather estimates were produced (as expected from a precipitation system), from RHI scans collected over a period of ~30 min. The majority of ρ_{hv} estimates are between 0.98 and 1, i.e., 91% of estimates with SNR $\geq$ 20 dB. This is expected from hydrometeors of the same type and it reflects on the high level of copolar H/V beam matching attained by the antenna. Furthermore, since these data were collected at different electronic steering angles along the vertical plane, this shows that beams are also well matched along the vertical cardinal plane. These observations are consistent with the results obtained in Section IV. Furthermore, element-level mutual coupling measurements are being recorded regularly and will be archived. In the future, we plan to analyze these measurements to quantify magnitude/phase drifts as a function of time, which impact polarimetric calibration and are a function of hardware stability.

Appendix

A. Model for Antenna Patterns

We present a succinct derivation on the basis of which the effects of mainlobes on the ρ_{hv} are evaluated. For characterizing antennas, the Ludwig 3 coordinate system [29] is convenient as it is tied to the antenna. Herein we use it as follows. The coordinate z we define along the beam center, the vertical coordinate we label as v and the horizontal coordinate perpendicular to both v and z we label with h (Fig. 12). To compute the polarimetric variable, one needs to evaluate integrals over the radar resolution volume V_6 centered at range r_0. V_6 is defined by the beam cross section and the range weighting function [15]. We will use the arc lengths $r_0 d\chi$ and $r_0 d\gamma$ for deriving various second order moments of voltages representing backscattered electric fields.

The angle γ is between the projection r_γ of the radial defining a point within the beam onto the v, z plane and the z axis (Fig. 12); the angle χ is between the projection of r_χ onto

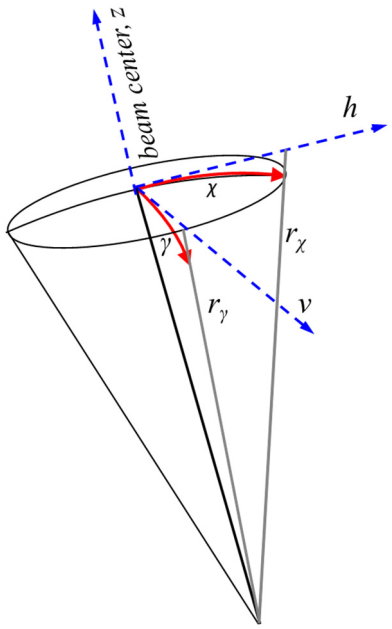

Fig. 12. Coordinate system used in defining various patterns and orientation of scatterers for deriving bias in ρ_{hv}. The view is from above the polarization plane (h, v). The beam center is along the coordinate z which is also the direction of propagation. The horizontal plane is defined with z, h. The vertical axis is v and the vertical plane is defined with v, h. The projection of a radial (not drawn) defining a point within the beam on the z, h plane is r_χ, and r_γ is a similar projection but on the z, v plane.

the *h, z* plane and the z axis. The elemental arcs we defined are orthogonal at the beam's center and almost orthogonal in the vicinity of the center. Consequently, we can assume orthogonality within pencil beams. The standard orthogonal system in Ludwig 3 consists of angle ϕ on a circle in the v, h plane centered on the z axis; θ is the angle between the z axis and a radial on the cone (the cone axis is along beam center). In that system a standard notation for a Gaussian main lobe one-way pattern [15] is

$$f^2(\theta,\phi) = \exp\left(-\frac{\theta^2}{4\sigma_\theta^2}\right) \quad \text{, for } \theta \in [0,\pi] \text{ and } \phi \in [0,2\pi], \tag{A1}$$

where σ_θ is the width of the two-way pattern, $f^4(\theta,\phi)$ and is related to the one way 3-dB width via $\theta_1 = 4\sqrt{\ln(2)}\sigma_\theta$, [15]. The integral of (A1) over the Gaussian lobe equals $\pi\theta_1^2/(8\ln 2)$ and is part of the weather radar equation (see [15], eq. 4.13).

Next, we demonstrate that the integral of (A1) over the angles θ,ϕ can be replaced with the integral over angles χ,γ of the function $f_{hh}^4(\chi,\gamma)$ which explicitly is

$$\int_{-\pi}^{\pi}\int_{-\pi}^{\pi} f_{hh}^4(\chi,\gamma) = \int_{-\infty}^{\infty}\int_{-\infty}^{\infty} \exp\left(-\frac{\chi^2}{2\sigma_{h\chi}^2} - \frac{\gamma^2}{2\sigma_{h\gamma}^2}\right) d\chi d\gamma, \tag{A2}$$

where the first index on f indicates the intended polarization, i.e., port for horizontal polarization is exited and horizontal polarization (second index) is achieved. This port also generates a vertically polarized wave through the cross polar pattern. That one we do not consider as our primary goal is to quantify the main lobe (copolar) effects. The first index on $\sigma_{h\chi}$ indicates the pattern corresponds to the horizontal polarization and the second indicates that $\sigma_{h\chi}$ is the pattern width along the χ angle (arc); similarly, $\sigma_{h\gamma}$ is the width of the pattern for horizontal polarization but along the almost perpendicular angle (arc) γ.The integration limits in (A2) have been extended to -∞, ∞ similarly to the limit of the (A1) integral. Assume circular pencil beam so $\sigma_{h\chi} = \sigma_{h\gamma} = \sigma_\theta$ and integrate (A2) to produce $2\pi\sigma_\theta^2 = \pi\theta_1^2/(8\ln 2)$ exactly same is the integral of (A1). We will use the expression for $f_{hh}^4(\chi,\gamma)$ in (A2) and an analogous one for the vertically polarized wave to compute the correlation coefficient.

We start with the transmitter voltages V_h^t, V_v^t for the H, V polarizations that generate incident electric fields on a scatterer located at $\mathbf{r}_i$ (range r_i, and angles χ_i, γ_i). To isolate the effects solely attributable to the main lobes we consider only the copolar scattering coefficients s_{hh} (in the h direction coincident with the arc χ) and s_{vv} (v direction coincident with the arc γ). We also ignore the cross polar pattern functions F_{hv} and F_{vh} and express incremental received voltages corresponding to a single scatterer as

$$\begin{vmatrix} \delta V_h \\ \delta V_v \end{vmatrix} = C \begin{vmatrix} F_{hh}^2(\chi_i,\gamma_i) w(r_i) s_{hh}(i) & 0 \\ 0 & F_{vv}^2(\chi_i,\gamma_i) w(r_i) s_{vv}(i) \end{vmatrix} \begin{bmatrix} V_h^t \\ V_v^t \end{bmatrix}, \tag{A3}$$

where index i identifies the scatterer and C contains the range dependence and other factors in the radar equation so that the right and left sides of (A3) are consistent and dimensionally correct. The pattern weighting functions for the two polarizations are

$$F_{hh}(\chi,\gamma) = \sqrt{g_h} f_h(\chi,\gamma) \tag{A4a}$$

and

$$F_{vv}(\chi,\gamma) = \sqrt{g_v} f_v(\chi,\gamma). \tag{A4b}$$

Antenna directivities are g_h, g_v, and f_h, f_v are normalized to their peaks. For compactness we use the following equalities and abbreviations

$$f_h^2(\chi,\gamma) = f_{h\chi}^2(x) f_{h\gamma}^2(y) = f_{h\chi}^2 f_{h\gamma}^2 = e^{-x^2/4\sigma_{h\chi}^2} e^{-y^2/4\sigma_{h\gamma}^2} \tag{A5a}$$

and

$$f_v^2(\chi,\gamma) = f_{v\chi}^2(x) f_{v\gamma}^2(y) = f_{v\chi}^2 f_{v\gamma}^2 = e^{-x^2/4\sigma_{v\chi}^2} e^{-y^2/4\sigma_{v\gamma}^2}. \tag{A5b}$$

The received voltages from scatterers principally inside the resolution volume are superposition of incremental voltages, therefore

$$V_h = C \sum_i F_{hh}^2 \chi_i, \gamma_i | w(r_i) | e^{-j4\pi r_i/\lambda} s_{hh}(i), \tag{A6}$$

similar expression holds for V_v.

We compute the correlation coefficient from the ensemble averages of the second order moments

$$\rho_{\rm hv} = \frac{\langle V_{\rm h}^* V_{\rm v}\rangle}{\langle |V_{\rm h}|^2\rangle^{1/2}\langle |V_{\rm v}|^2\rangle^{1/2}}. \tag{A7}$$

By definition the relation between the moment $\langle V_{\rm h}^* V_{\rm v}\rangle$ and the antenna radiation patterns is

$$\langle V_{\rm h}^* V_{\rm v}\rangle = C^2\Bigg\langle \sum_{i,j} F_{\rm hh}^2(\chi_{\rm i},\gamma_{\rm i}) F_{\rm vv}^2(\chi_{\rm i},\gamma_{\rm i}) |w(r_{\rm i})| \times |w(r_{\rm j})| e^{-j4\pi(r_{\rm j}-r_{\rm i}/\lambda} s_{\rm hh}^*(i) s_{\rm vv}(j)\Bigg\rangle. \tag{A8}$$

The range to the resolution volume center is r_0 and $w(r)$ is the range weighting function including sinusoidal dependence within the pulse, i.e., $w(r) = |w(r)|\exp(-j4\pi r/\lambda)$. The summation of $|w(r)|^2$ is over the interval δr centered on r_0 where $|w(r)|^2$ is substantial. For comparative purposes we assume scatterers are uniformly distributed, have locally invariant statistical properties and no differential phase upon scattering. Then $\langle s_{\rm hh}^*(i) s_{\rm vv}(i)\rangle = \langle s_{\rm hh} s_{\rm vv}\rangle$ and can be pulled out of the sum. After this simplification, commute the expectation and summation and separate the independent parts to express (A8) as

$$\langle V_{\rm h}^* V_{\rm v}\rangle = C^2\langle s_{\rm hh} s_{\rm vv}\rangle \sum_{i,j}\langle F_{\rm hh}^2(\chi_{\rm i},\gamma_{\rm i}) F_{\rm vv}^2(\chi_{\rm i},\gamma_{\rm i})\rangle \times \langle |w(r_{\rm i})||w(r_{\rm j})| e^{-j4\pi(r_{\rm j}-r_{\rm i})/\lambda}\rangle. \tag{A9}$$

Moreover, uniform distribution implies that differences $r_{\rm j}$-$r_{\rm i}$ are also uniformly distributed so that the second ensemble average in (A9) differs from zero only if $r_{\rm i} = r_{\rm j}$ (i.e., $i = j$) and this condition reduces the double sum to the single sum

$$\langle V_{\rm h}^* V_{\rm v}\rangle = C^2\langle s_{\rm hh} s_{\rm vv}\rangle \sum_{i} F_{\rm hh}^2(\chi_{\rm i},\gamma_{\rm i}) F_{\rm vv}^2(\chi_{\rm i},\gamma_{\rm i}) |w(r_{\rm i})|^2. \tag{A10}$$

Replace the sum with integrals (for details see [15], sec 4.4] over the resolution volume. The integral over the angles is separable from the integral over range; the latter one is a constant dependent on $w(r_{\rm i})$, which in turn is a function of the pulse shape and receiver impulse response [15] hence has no bearing on the correlation. Use the expressions in (A3) but for beam cross sections specific to each polarization, and write

$$\begin{aligned}\langle V_{\rm h}^* V_{\rm v}\rangle &\propto \langle s_{\rm hh} s_{\rm vv}\rangle g_{\rm h} g_{\rm v} \int_{-\infty}^{\infty}\int_{-\infty}^{\infty} f_{\rm h}^2(\chi,\gamma) f_{\rm v}^2(\chi,\gamma) d\chi d\gamma \\ &= \langle s_{\rm hh} s_{\rm vv}\rangle g_{\rm h} g_{\rm v} \int_{-\infty}^{\infty}\int_{-\infty}^{\infty} \exp\left(-\frac{\chi^2}{4\sigma_{\rm h\chi}^2} - \frac{\gamma^2}{4\sigma_{\rm h\gamma}^2}\right) \exp\left(-\frac{\chi^2}{4\sigma_{\rm v\chi}^2} - \frac{\gamma^2}{4\sigma_{\rm v\gamma}^2}\right) d\chi d\gamma \\ &= \langle s_{\rm hh} s_{\rm vv}\rangle g_{\rm h} g_{\rm v} \frac{4\pi\sigma_{\rm h\chi}\sigma_{\rm h\gamma}\sigma_{\rm v\chi}\sigma_{\rm v\gamma}}{\sqrt{\sigma_{\rm h\chi}^2+\sigma_{\rm v\chi}^2}\sqrt{\sigma_{\rm h\gamma}^2+\sigma_{\rm v\gamma}^2}}.\end{aligned} \tag{A11}$$

Via the same reasoning we get the moments in the denominator of (A4) yielding

$$\begin{aligned}\langle |V_{\rm h}|^2\rangle &\propto \langle s_{\rm hh}^2\rangle g_{\rm h} g_{\rm v} \int_{-\infty}^{\infty} \exp\left(-\frac{\chi^2}{2\sigma_{\rm h\chi}^2}\right) dx \int_{-\infty}^{\infty} \exp\left(-\frac{\gamma^2}{2\sigma_{\rm h\gamma}^2}\right) dy \\ &= \langle s_{\rm hh}^2\rangle g_{\rm h} g_{\rm v} 2\pi\sigma_{\rm h\chi}\sigma_{\rm h\gamma}\end{aligned} \tag{A12a}$$

and

$$\begin{aligned}\langle |V_{\rm v}|^2\rangle &\propto \langle s_{\rm vv}^2\rangle \int_{-\infty}^{\infty} \exp\left(-\frac{\chi^2}{2\sigma_{\rm v\chi}^2}\right) d\chi \int_{-\infty}^{\infty} \exp\left(-\frac{\gamma^2}{2\sigma_{\rm v\gamma}^2}\right) dy \\ &= \langle s_{\rm vv}^2\rangle g_{\rm h} g_{\rm v} 2\pi\sigma_{\rm v\chi}\sigma_{\rm v\gamma}.\end{aligned} \tag{A12b}$$

Substituting (A11), (A12a), and (A12b) in (A8) the correlation coefficient reduces to (A13a), as shown at the bottom of the page.

$$\begin{aligned}\rho_{\rm hv} = \frac{\langle s_{\rm hh} s_{\rm vv}\rangle}{\langle |s_{\rm hh}|^2\rangle^{1/2}\langle |s_{\rm vv}|^2\rangle^{1/2}} &= \frac{\int_{-\infty}^{\infty} f_{\rm h\chi}^2(\chi) f_{\rm v\chi}^2(\chi) d\chi \int_{-\infty}^{\infty} f_{\rm h\gamma}^2(\gamma) f_{\rm v\gamma}^2(\gamma) d\gamma}{\left[\int_{-\infty}^{\infty} f_{\rm h\chi}^4(\chi) d\chi \int_{-\infty}^{\infty} f_{\rm h\gamma}^4(\gamma) d\gamma\right]^{1/2}\left[\int_{-\infty}^{\infty} f_{\rm v\chi}^4(\chi) d\chi \int_{-\infty}^{\infty} f_{\rm v\gamma}^4(\gamma) d\gamma\right]^{1/2}} \\ &= \frac{\langle s_{\rm hh} s_{\rm vv}\rangle}{\langle |s_{\rm hh}|^2\rangle^{1/2}\langle |s_{\rm vv}|^2\rangle^{1/2}} \frac{2\sqrt{\sigma_{\rm h\chi}\sigma_{\rm h\gamma}\sigma_{\rm v\chi}\sigma_{\rm v\gamma}}}{\sqrt{\sigma_{\rm h\chi}^2+\sigma_{\rm v\chi}^2}\sqrt{\sigma_{\rm h\gamma}^2+\sigma_{\rm v\gamma}^2}}.\end{aligned} \tag{A13a}$$

$$\rho_{\rm hv} = \frac{\langle s_{\rm hh} s_{\rm vv}\rangle}{\langle |s_{\rm hh}|^2\rangle^{1/2}\langle |s_{\rm vv}|^2\rangle^{1/2}} = \frac{\int_{-\infty}^{\infty} f_{\rm h}^2(\chi) f_{\rm v}^2(\chi) d\chi \int_{-\infty}^{\infty} f_{\rm h}^2(\gamma) f_{\rm v}^2(\gamma) d\gamma}{\left[\int_{-\infty}^{\infty} f_{\rm h}^4(\chi) d\chi \int_{-\infty}^{\infty} f_{\rm h}^4(\gamma) d\gamma\right]^{1/2}\left[\int_{-\infty}^{\infty} f_{\rm v}^4(\chi) d\chi \int_{-\infty}^{\infty} f_{\rm v}^4(\gamma) d\gamma\right]^{1/2}}. \tag{A13b}$$

$$\xi = \frac{\int_{-\infty}^{\infty} f_{\rm h}^2(\chi) f_{\rm v}^2(\chi) d\chi \int_{-\infty}^{\infty} f_{\rm h}^2(\gamma) f_{\rm v}^2(\gamma) d\gamma}{\left[\int_{-\infty}^{\infty} f_{\rm h}^4(\chi) d\chi \int_{-\infty}^{\infty} f_{\rm h}^4(\gamma) d\gamma\right]^{1/2}\left[\int_{-\infty}^{\infty} f_{\rm v}^4(\chi) d\chi \int_{-\infty}^{\infty} f_{\rm v}^4(\gamma) d\gamma\right]^{1/2}}. \tag{A14}$$

Introducing the compact notation (6a) and (6b) further simplifies (A13a) to (A13b), as shown at the bottom of the previous page.

As explained in the main text the intrinsic ρ_{hvi} is the fraction containing the ensemble averages of scattering coefficients products. The second fraction with integrals over the pattern lobes is the fractional bias ξ caused by the patterns (A14), as shown at the bottom of the previous page.

ACKNOWLEDGMENT

This work is supported mostly by NOAA/Office of Oceanic and Atmospheric Research under NOAA-University of Oklahoma Cooperative Agreement #NA21OAR4320204, U.S. Department of Commerce. Any opinions, findings, and conclusions or recommendations expressed in this paper are those of the author(s), and do not necessarily reflect the views of NOAA. Larry Hopper's corrections and suggestions have improved the paper. The authors would like to thank the ARRC engineers for the design and development efforts that resulted in the Horus radar.

REFERENCES

[1] D. S. Zrnic et al., "Agile-beam phased array radar for weather observations," *Bull. Amer. Meteorol. Soc.*, vol. 88, no. 11, pp. 1753–1766, Nov. 2007.

[2] A. V. Ryzhkov and D. S. Zrnic, *Radar Polarimetry for Weather Observations*. Cham, Switzerland: Springer, 2019.

[3] J. D. Díaz et al., "A cross-stacked radiating antenna with enhanced scanning performance for digital beamforming multifunction phased-array radars," *IEEE Trans. Antennas Propag.*, vol. 66, no. 10, pp. 5258–5267, Oct. 2018.

[4] I. Ivic et al., "An overview of weather calibration for the advanced technology demonstrator," in *Proc. IEEE Int. Symp. Phased Array Syst. Technol. (PAST)*, Oct. 2019, pp. 1–7.

[5] M. Galletti and D. S. Zrnic, "Bias in copolar correlation coefficient caused by antenna radiation patterns," *IEEE Trans. Geosci. Remote Sens.*, vol. 49, no. 6, pp. 2274–2280, Jun. 2011.

[6] A. Ryzhkov and J. Krause, "New polarimetric radar algorithm for melting-layer detection and determination of its height," *J. Atmos. Ocean. Technol.*, vol. 39, no. 5, pp. 529–543, May 2022.

[7] K. L. Ortega, J. M. Krause, and A. V. Ryzhkov, "Polarimetric radar characteristics of melting hail. Part III: Validation of the algorithm for hail size discrimination," *J. Appl. Meteorol. Climatol.*, vol. 55, no. 4, pp. 829–848, Apr. 2016.

[8] R. D. Palmer et al., "Horus—A fully digital polarimetric phased array radar for next-generation weather observations," *IEEE Trans. Radar Syst.*, vol. 1, pp. 96–117, 2023.

[9] R. Palmer et al., "A primer on phased array radar technology for the atmospheric sciences," *Bull. Amer. Meteorol. Soc.*, vol. 103, no. 10, pp. E2391–E2416, 2022.

[10] I. R. Ivić, "An approach to simulate the effects of antenna patterns on polarimetric variable estimates," *J. Atmos. Ocean. Technol.*, vol. 34, no. 9, pp. 1907–1934, Sep. 2017.

[11] C. Fulton, P. Clough, V. Pai, and W. Chappell, "A digital array radar with a hierarchical system architecture," in *IEEE MTT-S Int. Microw. Symp. Dig.*, Jun. 2009, pp. 89–92.

[12] C. Fulton, M. Yeary, D. Thompson, J. Lake, and A. Mitchell, "Digital phased arrays: Challenges and opportunities," *Proc. IEEE*, vol. 104, no. 3, pp. 487–503, Mar. 2016.

[13] M. Yeary, R. Palmer, C. Fulton, J. Salazar-Cerreno, and H. Sigmarsson, "Preliminary chamber measurements and a status report on the development of an all-digital mobile phased array radar," in *Proc. IEEE Radar Conf. (RadarConf)*, Mar. 2022, pp. 1–5.

[14] D. Schvartzman, J. D. D. Diaz, D. Zrnic, M. Herndon, M. B. Yeary, and R. D. Palmer, "Holographic back-projection method for calibration of fully digital polarimetric phased array radar," *IEEE Trans. Radar Syst.*, 2023.

[15] R. J. Doviak and D. Zrnic, *Doppler Radar and Weather Observations*. Mineola, NY, USA: Dover, 2006.

[16] D. Schvartzman, S. M. Torres, and T. Yu, "Motion-compensated steering: Enhanced azimuthal resolution for polarimetric rotating phased array radar," *IEEE Trans. Geosci. Remote Sens.*, vol. 59, no. 12, pp. 10073–10093, Dec. 2021.

[17] C. A. Balanis, *Antenna Theory: Analysis and Design*. Hoboken, NJ, USA: Wiley, 2015.

[18] D. Schvartzman et al., "A polarimetric antenna-calibration method for the Horus radar based on E-field back projection," in *Proc. IEEE Int. Symp. Phased Array Syst. Technol. (PAST)*, Oct. 2022, pp. 1–7.

[19] J. L. Salazar, N. Aboserwal, J. D. Díaz, J. A. Ortiz, and C. Fulton, "Edge diffractions impact on the cross polarization performance of active phased array antennas," in *Proc. IEEE Int. Symp. Phased Array Syst. Technol. (PAST)*, Oct. 2016, pp. 1–5.

[20] I. R. Ivić and D. Schvartzman, "A first look at the ATD data corrections," in *Proc. 39th Int. Conf. Radar Meteorol.*, 2019.

[21] D. S. Zrnic, V. M. Melnikov, and R. J. Doviak, "Issues and challenges for polarimetric measurement of weather with an agile beam phased array radar," NOAA/NSSL, Norman, OK, USA, Tech. Rep., 2012, p. 117.

[22] J. A. Ortiz, "Impact of edge diffraction in dual-polarized phased array antennas," Ph.D. dissertation, Univ. Oklahoma, Norman, OK, USA, 2020.

[23] D. Zrnić, R. Doviak, G. Zhang, and A. Ryzhkov, "Bias in differential reflectivity due to cross coupling through the radiation patterns of polarimetric weather radars," *J. Atmos. Ocean. Technol.*, vol. 27, no. 10, pp. 1624–1637, Oct. 2010.

[24] NOAA/NWS, Washington, DC, USA. (2015). *Radar Functional Requirements [Report]*. [Online]. Available: https://www.roc.noaa.gov/WSR88D/PublicDocs/NOAA_Radar_Functional_Requirements_Final_Sept%202015.pdf

[25] J. D. Díaz, "Ultra-low cross-polarization antenna architectures for multifunction planar phased arrays," Ph.D. dissertation, Univ. Oklahoma, Norman, OK, USA, 2021.

[26] C. Fulton et al., "Mutual coupling-based calibration for the Horus digital phased array radar," in *Proc. IEEE Int. Symp. Phased Array Syst. Technol. (PAST)*, Oct. 2022, pp. 1–6.

[27] C. M. S. Aquino, B. Cheong, and R. D. Palmer, "Progressive pulse compression: A novel technique for blind range recovery for solid-state radars," *J. Atmos. Ocean. Technol.*, vol. 38, no. 9, pp. 1599–1611, Jul. 2021.

[28] C. M. Salazar, B. Cheong, R. D. Palmer, D. Schvartzman, and A. Ryzhkov, "Salient improvements in the progressive pulse compression technique," *J. Atmos. Oceanic Technol.*, 2023.

[29] A. Ludwig, "The definition of cross polarization," *IEEE Trans. Antennas Propag.*, vol. AP-21, no. 1, pp. 116–119, Jan. 1973.

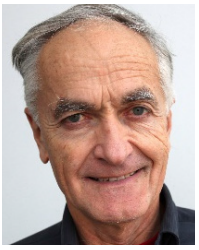

Dušan S. Zrnić (Life Fellow, IEEE) received the bachelor's degree from the University of Belgrade, Belgrade, Serbia, in 1965, and the M.S. and Ph.D. degrees from the University of Illinois at Urbana–Champaign, Champaign, IL, USA, in 1966 and 1969, respectively.

He is currently a Senior Scientist with the National Severe Storms Laboratory, Norman, OK, USA, and an Affiliate Professor of meteorology and electrical engineering, The University of Oklahoma, Norman. He has developed several scientific and engineering aspects of polarimetric weather radar technology leading to implementation on the WSR-88Ds. He was inducted into the U.S. National Academy of Engineering in 2006 for the development of potent radar methods that have greatly enhanced operational weather detection and warning and advanced meteorological research. He is currently a fellow of AMS. He was a recipient of the AMS Remote Sensing Prize in 2008 for pioneering and substantial contributions to the improvements of meteorological radars for both research and operational applications. He was the Chief Editor of the *Journal of Atmospheric and Oceanic Technology*.

David Schvartzman (Senior Member, IEEE) was born in Piracicaba, Brazil, in 1988. He received the B.S. degree in electrical and computer engineering from the National University of Asunción, San Lorenzo, Paraguay, in 2011, and the M.S. and Ph.D. degrees in electrical and computer engineering from The University of Oklahoma, Norman, OK, USA, in 2015 and 2020, respectively.

From 2015 to 2020, he was a Research Scientist with the NOAA National Severe Storms Laboratory (NSSL) and the Cooperative Institute for Severe and High-Impact Weather Research and Operations (CIWRO). From 2021 to 2022, he was a Research Scientist with the Advanced Radar Research Center (ARRC), The University of Oklahoma, where he is currently an Assistant Professor with the School of Meteorology, affiliated with the ARRC. He works on novel signal processing algorithms to improve understanding of atmospheric processes using phased array radar. He also works on calibration and integration of phased array radar systems. He is a member of the American Meteorological Society (AMS). He was a recipient of the 2019 American Meteorological Society's Spiros G. Geotis Prize.

Robert D. Palmer (Fellow, IEEE) was born in Fort Benning, GA, USA, in 1962. He received the Ph.D. degree in electrical engineering from The University of Oklahoma (OU), Norman, OK, USA, in 1989.

From 1989 to 1991, he was a JSPS Post-Doctoral Fellow with the Radio Atmospheric Science Center, Kyoto University, Japan, where his major accomplishment was the development of novel interferometric radar techniques for studies of atmospheric turbulent layers. After his stay in Japan, he was with the Physics and Astronomy Department, Clemson University, Clemson, SC, USA. From 1993 to 2004, he was a part of a Faculty Member with the Department of Electrical Engineering, University of Nebraska–Lincoln, where his interests broadened into areas including wireless communications, remote sensing, and pedagogy. Soon after moving to OU as the Tommy C. Craighead Chair with the School of Meteorology in 2004, he established the interdisciplinary Advanced Radar Research Center (ARRC). He currently serves as the Executive Director of the ARRC and OU's Associate Vice President for Research and Partnerships. While at OU, his research interests have focused on the application of advanced radar signal processing techniques to observations of severe weather, particularly related to phased-array radars and other innovative system designs. He has published widely in the area of radar sensing of the atmosphere, with over 115 peer-reviewed journal articles, one textbook, 40 international invited talks, and over 300 conference presentations. He is a fellow of the American Meteorological Society (AMS) emphasizing his dedication to the interdisciplinary nature of radar science.

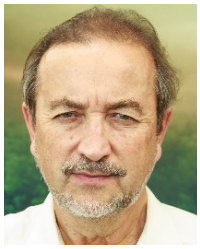

Alexander V. Ryzhkov received the M.S. and Ph.D. degrees in radio science from Leningrad State University, Saint Petersburg, Russia, in 1974 and 1977, respectively. From 1978 to 1992, he was with the Main Geophysical Observatory, Leningrad, Russia. In 1992, he joined the National Severe Storms Laboratory, Norman, OK, USA, and the Cooperative Institute for Mesoscale Meteorological Studies, The University of Oklahoma, Norman, where he has been a Senior Research Scientist since 1995. In 2021, the Institute became Cooperative Institute for Severe and High-Impact Weather Research and Operations. He contributed extensively to the development of polarimetric radar algorithms for quantitative precipitation estimation, hydrometeor classification, and microphysical retrievals and their operational applications on the U.S. National Weather Service WSR-88D weather radar network. His current research interests include atmospheric remote sensing, radiowave propagation, cloud microphysics, and radar meteorology with a focus on Doppler polarimetric radars.